



Chemical discrimination of the particulate and gas phases of miniCAST exhausts using a two-filter collection method

Linh Dan Ngo^{1,2}, Dumitru Duca¹, Yvain Carpentier¹, Jennifer A. Noble^{1,*}, Raouf Ikhenazene¹, Marin Vojkovic¹, Cornelia Irimiea³, Ismael K. Ortega³, Guillaume Lefevre⁴, Jérôme Yon⁴, Alessandro Faccineto², Eric Therssen², Michael Ziskind¹, Bertrand Chazallon¹, Claire Pirim¹, Cristian Focsa¹

¹Univ. Lille, CNRS, UMR 8523 – PhLAM – Laboratoire de Physique des Lasers Atomes et Molécules, F-59000 Lille, France

²Univ. Lille, CNRS, UMR 8522 – PC2A – Physicochimie des Processus de Combustion et de l'Atmosphère, F-59000 Lille, France

³ONERA – The French Aerospace Laboratory, F-91123 Palaiseau, France

⁴Normandie Univ., INSA Rouen, UNIROUEN, CNRS, CORIA, 76000 Rouen, France

* now at: CNRS, Aix Marseille Université, PIIM, UMR 7345, 13397 Marseille cedex, France

Correspondence to: Yvain Carpentier (yvain.carpentier@univ-lille.fr)

Abstract. Combustion of hydrocarbons produces both particulate and gas phase emissions responsible for major impacts on atmospheric chemistry and human health. Ascertaining the impact of these emissions, especially on human health, is not straightforward because of our relatively poor knowledge of how chemical compounds are partitioned between the particle and gas phases. Accordingly, we propose to couple a two-filter sampling method with a multi-technique analytical approach to fully characterize the particulate and gas phase compositions of combustion by-products. The two-filter sampling method is designed to retain particulate matter (elemental carbon possibly covered in a surface layer of adsorbed molecules) on a first quartz fiber filter while letting the gas phase pass through, and then trap the most volatile components on a second black carbon-covered filter. All samples thus collected are subsequently subjected to a multi-technique analytical protocol involving two-step laser mass spectrometry (L2MS), secondary ion mass spectrometry (SIMS), and micro-Raman spectroscopy. Using the combination of this two-filter sampling/multi-technique approach in conjunction with advanced statistical methods we are able to unravel distinct surface chemical compositions of aerosols generated with different set points of a miniCAST burner. Specifically, we successfully discriminate samples by their volatile, semi-volatile and non-volatile polycyclic aromatic hydrocarbon (PAH) contents and reveal how subtle changes in combustion parameters affect particle surface chemistry.

1 Introduction

Particulate matter (PM) produced by incomplete combustion of hydrocarbon-based fuels is often found associated to gas phase compounds that include carbon and nitrogen oxides (CO, CO₂, and NO_x), along with a volatile fraction of organic species encompassing low-mass polycyclic aromatic hydrocarbons (PAHs). The presence of PAHs in the atmosphere is of



great concern due to their carcinogenic and mutagenic potential (Kim et al., 2013). In fact, in the current European air quality legislation (European Fourth Air quality Daughter Directive 2004/107/EC), seven potentially harmful PAHs at least have to be monitored, but restrictions on PAH concentrations are currently solely limited to benzo[a]pyrene because of its recognized high toxicity (annual target value of 1 ng m^{-3} in the PM₁₀ particulate phase fraction (Pandey et al., 2011)).

35 However, it is a conjunction of the PM intrinsic physico-chemical properties (e.g. nature of adsorbed PAH – Dachs and Eisenreich, 2000 – or water affinity) with pressure, temperature, hygrometric variations or ageing processes in the atmosphere that ultimately condition phase partitioning (free vs bound fraction, Ravindra et al., 2006). Consequently, relatively abundant gas-phase PAHs – yet known to bear only weak carcinogenic or mutagenic effects (Nisbet and LaGoy,

40 1992) – can further react through gas-phase processes or heterogeneous gas-PM exchanges to produce noxious oxy- or nitro-PAHs for instance (Atkinson and Arey, 1994; Bandowe et al., 2014). PAHs emitted in exhausts, in either the gas phase or the particulate phase must be analyzed and fully characterized at the same time to better understand their deposition mechanism or chemical transformation in the atmosphere and help ascertain their overall toxicity and impact on human health.

45 Several methods allowing the concomitant sampling of airborne PAHs in both the gas and particulate phases have been developed in the last decade (see e.g. the reviews by Pandey et al., 2011; Szulejko et al., 2014). The sampling protocol starts with the choice of a suitable sorbent material to either solely capture the vapor phase or solely retain PM. The former sorbent material mostly consists of polyurethane foam, resins, or graphitized carbon black mesh, whereas the latter are rather made of glass fiber, quartz fiber, or Teflon filters. The sorbents are placed in series, i.e. one after the other in the exhaust line. The

50 soluble organic fraction is then extracted off-line from the sorbent (filter and/or resin) for subsequent gas chromatography mass spectrometry (GC-MS) analyses (An et al., 2016; Elghawi et al., 2010; Sun et al., 2006). However, such solvent extraction methods exhibit recovery rates that are highly dependent upon the technique applied and the nature of PAHs a priori present. Accordingly, the GC-MS method, which relies on solvent extraction methods and calibration standards, is a time-consuming technique which is inherently more sensitive towards compounds having the greatest solubility. To

55 circumvent this limitation, solvent-free methods have been recently developed based on thermal desorption (e.g. Villanueva et al., 2018), microwave-assisted desorption, or solid-phase micro-extraction (Szulejko et al., 2014). However, because sampling substrates may differ for PM and gas trapping, and often necessitate extraction techniques before characterization whose efficiencies are substrate-dependent, results obtained for the two phases may be difficult to compare and do not necessarily represent the whole PAH family making up either filter.

60 The CAST (Combustion Aerosol Standard) generator is often chosen to produce combustion-generated particles as it is easy to implement for systematic laboratory experiments, the fuel and oxidation air flows being easily modifiable, and hence enables the investigation of a variety of chemistries which can mimic some of the physico-chemical properties of soot particles emitted by real engines (as the ones from aircrafts or cars, e.g. Bescond et al., 2014; Moore et al., 2014). Time-of-Flight Aerosol Mass Spectrometry (ToF-AMS) has been used in the past by Ferge et al. (2006) and Mueller et al. (2015) to

65 study PAH formation in the CAST generator at different oxidation flows. However, because the sample thus generated are



particles, no information about the gas phase composition can be derived in these experiments, which provide only an incomplete picture of the PAH family emitted in the exhausts.

In this work, we coupled a two-filter sampling method with a multi-technique analytical approach to fully characterize the particulate and gas phase compositions of combustion by-products. The two-filter collection method intends to separate the particulate phase (Front Filter) from the gas phase (Back Filter) using fibrous filtration media (Quartz Fiber Filters – QFF).
70 Once collected, the filters are analyzed using a multi-technique approach encompassing two-step laser mass spectrometry (L2MS), secondary ion mass spectrometry (SIMS), and micro-Raman spectroscopy. The L2MS technique has been extensively developed in our group (at the University of Lille/PhLAM laboratory) over the last decade to specifically probe the chemical composition of combustion byproducts (Delhaye et al., 2017; Faccinetto et al., 2011, 2015; Moldanová et al.,
75 2009; Popovicheva et al., 2017). Its high sensitivity and selectivity towards specific classes of compounds owing to different ionization schemes makes it an extremely valuable analytical tool that can be adapted to various samples. Using three different ionization wavelengths, it is possible to target various classes of compounds and reach sub-fmol limit of detection, e.g. for PAHs (Faccinetto et al., 2008, 2015). The laser desorption process along with its coupling with the subsequent ionization step have been optimized over the years (Faccinetto et al., 2008; Mihešan et al., 2006, 2008) and ensure a soft
80 removal (with minimum internal energy excess) of molecules adsorbed on the particle surface, while avoiding/limiting both their fragmentation and the in-depth damaging of the underlying carbon matrix (Faccinetto et al., 2015). L2MS spectra obtained in this work are additionally backed with the SIMS spectra of deposited CAST PM, with no sample preparation prior to the analyses since the particulate matter is preferentially trapped on the Front Filter. Subtle differences and similarities between Front and Back Filters are revealed after mass spectrometry results (L2MS and SIMS) using the recently
85 developed advanced statistical methodologies (Irimiea et al., 2018, 2019) based on principal component analysis (PCA).

2 Experimental methods

2.1 Sample collection

PM were sampled from the exhausts of a miniCAST generator (5201c) from Jing Ltd., as described previously in e.g. Yon et al. (2018). Briefly, the miniCAST contains a propane-nitrogen flame with operating conditions controlled by the flow rates
90 of propane, nitrogen, oxidation air (Q^{air}) and dilution air. The working points used in this study (and others in this series Bescond et al., 2014; Ouf et al., 2016; Yon et al., 2015) are detailed in Fig. 1. The main difference between these working points is the oxidation air flow and – for the SP4 point – nitrogen dilution, with an increasing oxidation air flow in the order $Q^{\text{air}}_{\text{SP3}} < Q^{\text{air}}_{\text{SP2}} < Q^{\text{air}}_{\text{SP4}} < Q^{\text{air}}_{\text{SP1}}$. The samples were deposited on quartz fiber filters (QFF, Pall Tissuquartz QAT-UP 2500) using a specially designed sampling line (as illustrated in Fig. 1). A line derivation parallel to the sampling system has been
95 added to ensure the CAST is maintained at atmospheric pressure. These QFF are typically used in soot collection, for example in studies of aircraft PM (Delhaye et al., 2017), and are also employed when deriving organic carbon to total carbon (OC/TC) values of deposited soot (Bescond et al., 2016; Yon et al., 2015). QFF are chosen because they proved to be highly



efficient in capturing combustion emissions and they have a stable penetration curve among other filters when a range of physical parameters are varying in the sampling line (Zíková et al., 2015). From a theoretical point of view, it is very difficult to predict the collection efficiency of QFF for particles within the nanometer size domain, as generated in our combustion conditions (e.g. 99–166 nm modal diameter, Bescond et al., 2016). Filter collection efficiency is directly related to inertial impaction, direct interception, Brownian diffusion and electrostatic forces (Brochot et al., 2019; Lindsley, 2016; Zíková et al., 2015). The resulting component of these forces is translated into a function that displays near 100 % collection efficiency for particles smaller than 20 nm and larger than 300 nm. The minimum collection efficiency, which is also referred to as the most penetrating particle size (MPPS), is obtained for the 100–300 nm size range. However, some studies showed that the MPPS for QFF may peak around 60 nm and are possibly < 100 nm for other fibrous media (Brochot et al., 2019; Zíková et al., 2015). While this measured values are mostly influenced by both the flow velocity in the sampling line and the pressure drop at the surface of the filter, our flow conditions are close to those used in the work of Zíková et al. (2015). Consequently, we can roughly estimate that the MPPS for the “Front filter” is below 100 nm. Two filters were used for each sampling period: the “Front Filter” was a bare QFF placed in the exhaust line; the “Back Filter” was a QFF covered with a thin layer of black carbon (Pureblack 100 Carbon, Columbian Chemicals Company, specific surface 80–150 m² g⁻¹) and placed 3.5 cm downstream of the Front Filter in the sampling line. Prior to sampling, the Back Filter was heated in an oven at 150°C for 16 hours to remove pre-adsorbed species. Back Filters thus produced were shown to yield no signal when analyzed by L2MS. Black carbon has previously been used as a matrix upon which pure PAHs were adsorbed for mass spectrometric analysis of soot surrogates (Faccineto et al., 2011, 2015). In the same studies, black carbon-covered filters were also used to sample the volatile fraction in flames. In the present study, the sampling line was designed to collect PM (including adsorbed species) on the Front Filter and to trap gas phase molecules from the remaining exhaust on the Back Filter. Sampling was performed for 20 minutes per working point. ‘Reference’ samples (Front and Back Filters) were collected by running the miniCAST generator for only two minutes under set point SP1 conditions. These samples represent pre-stabilization burner conditions. They were collected as ‘reference’ to ensure that the samples were not impacted by this early combustion phase. The loading on these ‘reference’ samples was much lower. After collection, samples were placed in watch glasses covered with Al foil, and stored at 4°C before analysis.

2.2 Two-step (desorption / ionization) laser mass spectrometry

Samples were analyzed using a two-step laser mass spectrometry (L2MS) technique built in-house (Mihešan et al., 2008). Briefly, the soot sample is introduced into the analysis chamber (10⁻⁸ mbar) via a preparation chamber, where it is pre-cooled by a constant flow of liquid nitrogen in the sample holder to avoid the sublimation of the most volatile species. In the analysis chamber of the time-of-flight mass spectrometer (ToF-MS), the sample is irradiated at normal incidence by the beam of a frequency-doubled Nd:YAG laser (Continuum Minilite, $\lambda_d = 532$ nm, 4 ns pulsewidth) shaped using a circular aperture and a 10 cm focal length plano-convex CaF₂ lens to form a beam with homogeneous fluence, 0.8 mm-diameter spot on the sample surface. Such irradiation is known to induce the desorption of neutral species from soot without affecting the



carbon matrix (Faccinnetto et al., 2008). All samples were analyzed with same desorption conditions ($\lambda_d = 532$ nm, $400 \mu\text{J pulse}^{-1}$, 80 mJ cm^{-2} i.e. 20 MW cm^{-2}).

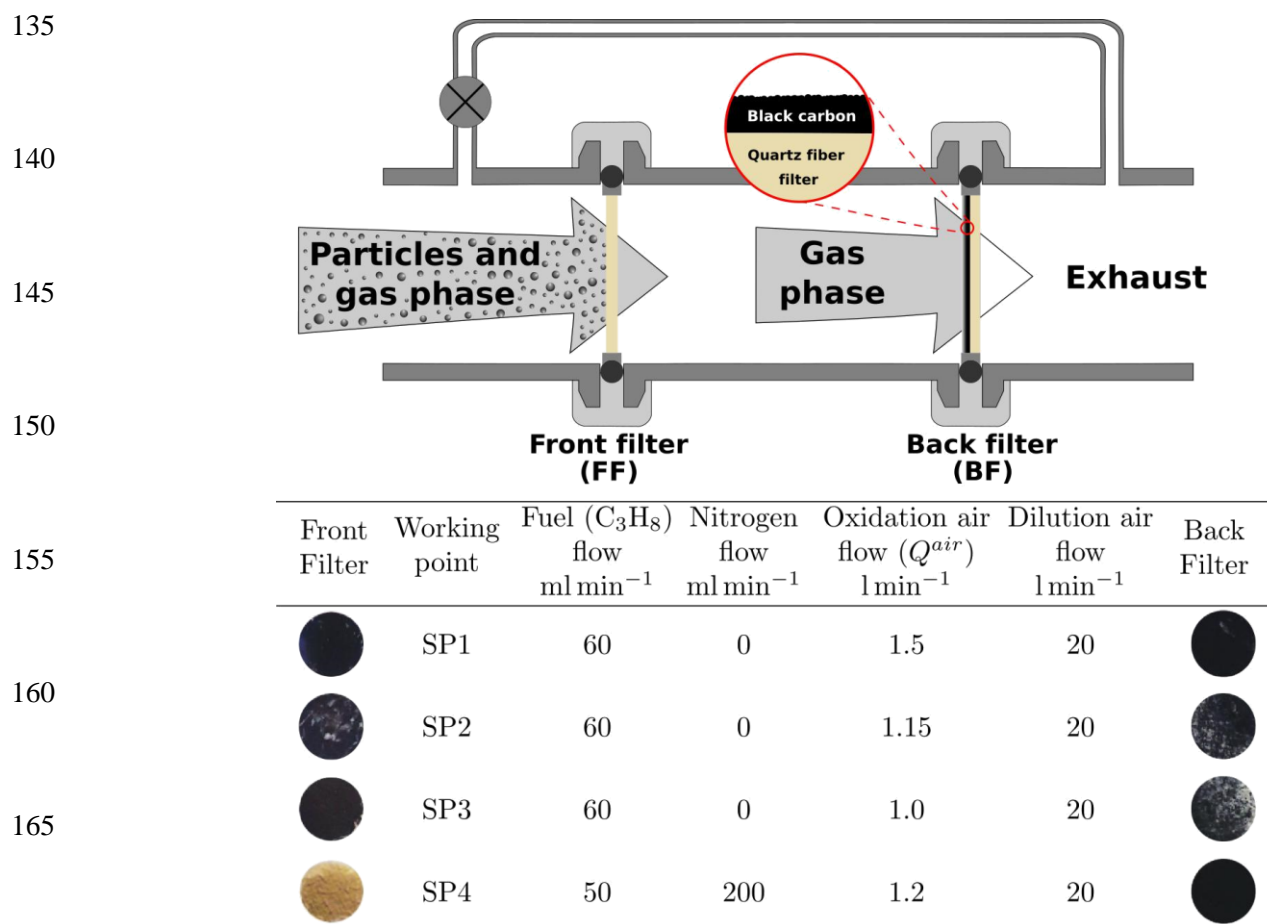


Figure 1. Schematic of the sampling line and photos of sampled soot. The combustion parameters for the miniCAST burner are presented in the table.

The desorbed plume propagates normally from the sample surface towards the extraction plates of the ToF-MS. The molecules from the desorbed plume are then ionized by either a resonant two-photon ionization R2PI (Zimmermann et al., 2001) process at $\lambda_i = 266$ nm (4 ns-width pulsed UV laser, Continuum Powerlite, 1 mJ pulse^{-1}) or a single photon ionization (SPI) process at $\lambda_i = 157$ nm (5 ns-width pulsed VUV excimer laser, Coherent ExciStar XS 200) or $\lambda_i = 118$ nm (in-house built coherent nanosecond source). The ninth harmonic of the Nd:YAG laser ($\lambda_i = 118.2$ nm) was generated by tripling the 355 nm output of a Continuum Surelite pulsed laser in a Xe cell (Hilbig, 1982; Popovicheva et al., 2017). For the two SPI wavelengths, the setup was optimized to the maximum output (i.e. maximum electric potential for the 157 nm excimer laser,



185 and maximum pumping energy for the 355 nm laser (34 mJ pulse⁻¹) to maximize 118 nm conversion, at an estimated conversion efficiency of 0.01 % (Butcher, 1999). The time delay between desorption and ionization is set to 100 μs by a digital delay/pulse generator (Stanford DG535). Generated ions are then mass analyzed in a 1.72 m-long reflectron ToF-MS (RM Jordan) with a mass resolution of $m/\Delta m$ 1000. Ion detector signals are recorded using a digital oscilloscope (LeCroy Waverunner 9350AM) at a time resolution of 4 ns/point. Each spectrum corresponds to an average of at least 200 desorption shots at different locations on the sample. A set of 5 spectra was obtained for each CAST sample (FF and BF) and each ionization scheme. Therefore, in total, 30 spectra were obtained for each CAST set point.

2.3 Secondary ion mass spectrometry

190 Time-of-Flight Secondary Ion Mass Spectrometry analysis was conducted with TOF.SIMS⁵ instrument from ION-TOF GmbH. Briefly, samples were introduced into the analysis chamber with a residual pressure of 10⁻⁸ mbar. The sample surface was bombarded by a 25 keV Bi₃⁺ ion beam with a current of 0.3 pA in static mode. A 180 s acquisition time and 25 random scans/acquisition were used for an analyzed area of 500 μm × 500 μm on the sample surfaces. Mass spectra were collected in both positive and negative polarities for at least three areas per sample. The mass resolution at m/z 29 is approximately 2700. For this analysis samples are not cooled down. Ion signals in SIMS mass spectra were identified and calibrated using SurfaceLab 6 software from ION-TOF GmbH. Positive spectra were calibrated with peaks C⁺ (m/z 12.000), CH₃⁺ (m/z 15.023), C₇H₇⁺ (m/z 91.055), C₁₆H₁₀⁺ (m/z 202.078), and C₁₉H₁₁⁺ (m/z 239.086). Negative spectra were calibrated with peaks at C⁻ (m/z 12.000), CH⁻ (m/z 13.008), O⁻ (m/z 15.995), C₂⁻ (m/z 24.000), C₄H⁻ (m/z 49.008), and C₈H⁻ (m/z 97.008). A set of 5 spectra was obtained for each CAST sample (FF and BF) and each polarity. Therefore, in total, 20 spectra were acquired for each CAST set point.

2.4 Raman micro-spectroscopy

205 Raman analyses were performed with an Invia reflex spectrometer (Renishaw) equipped with an Olympus microscope (BXFM) (Chazallon et al., 2014). The spectra presented in this work were obtained by irradiation with a 514 nm laser with a nominal power of 150 mW. The laser power was reduced to avoid thermal effects at the sample surface. Using a lens with 20× magnification (N.A. 0.5), the laser was focused on the sample surface with a spot of 3.0 μm diameter. The spectrometer was calibrated using the Stokes Raman signal of pure Si at 520 cm⁻¹. Raman spectra of spectral resolution 12 cm⁻¹ were collected at four different spots on each sample using integration times of 60 s with 10–20 scans accumulated per spectrum.

2.5 Multivariate data analysis: principal component analysis (PCA)

210 PCA is a technique used to highlight variation and patterns in a data set, and in this case was used to reveal the differences in chemical composition of the samples, and in particular between (i) Front and Back Filters and (ii) miniCAST set points. PCA is very convenient to outline the subtle differences between data sets, since it reduces the dimensionality of complex data while preserving most of the information. PCA was applied to each of the five datasets (3 L2MS ionization wavelengths



and 2 SIMS polarities) following the procedure detailed in Popovicheva et al. (2017), Irimiea et al. (2018), and Duca et al. (2019). Further information can also be found in Sect. S2. Briefly, each mass spectrum was represented by a set of values
215 corresponding to the integrated area of a selected number of mass peaks in the spectrum. The number of selected mass peaks was 66, 105, and 60 in L2MS mass spectra recorded at $\lambda_i = 266, 157,$ and 118 nm, respectively, and 138 and 70 in SIMS mass spectra recorded in positive and negative polarity, respectively. PCA analyses were performed using a covariance matrix, i.e. each data set was organized into a matrix containing observations/samples (arranged in rows) and variables/peak integrated area (arranged in columns). Principal components (PCs) were constructed as linear combinations or mixtures of
220 the initial variables (peak integrated areas). The physical meaning of all derived PCs can be inferred from the contribution of the various molecular species to the loadings, i.e. by determining the relative importance of each mass peak integrated area to the main variance in the data set. Scree plots and loadings for all L2MS PCA analyses discussed in this article can be found in the supplementary material (Fig. S2 and S3). It should be further noted that initial PCA tests included ‘reference’ samples (in both L2MS and SIMS PCAs). This preliminary step resulted in PC1 (the largest variance in the data set) being
225 dominated by the variance between the ‘reference’ samples (Front and Back Filters) and all other samples, confirming that the early pre-stabilization deposition does not influence the spectra of the various set points measured. After this confirmation step, the ‘reference’ samples were removed from the covariance matrix used to perform the PCA and therefore are not presented in the following sections.

3 Results and Discussion

3.1 L2MS analysis

3.1.1 Mass spectra obtained by L2MS at individual ionization wavelengths

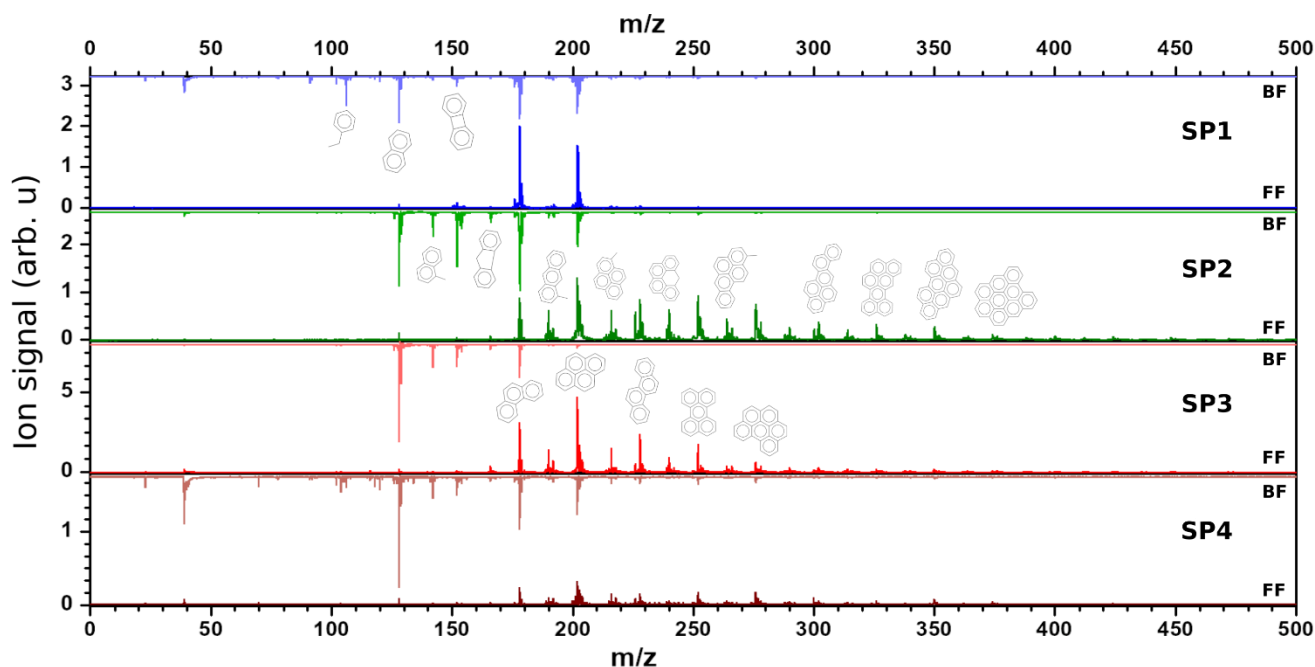
L2MS mass spectra of samples SP1, SP2, SP3, and SP4 (for both Front and Back Filters) produced at three different ionization wavelengths (266, 157, and 118 nm) are discussed in this section. Mass spectra obtained with a 266 nm ionization wavelength are presented in Fig. 2, whereas results obtained for 157 and 118 nm are both presented in Fig. S1.
235

Upon 266 nm ionization, all mass spectra are dominated by signals attributed to aromatic species, and more specifically PAHs (Fig. 2). An important advantage of L2MS is to generate, for the most part, fragment-free mass spectra while maintaining a high signal-to-noise ratio, due to the controlled desorption and ionization fluences (Faccinetto et al., 2011). On all mass spectra generated with a 266 nm ionization wavelength, the lightest detected PAH is naphthalene ($C_{10}H_8^+$, m/z 128).

240 On Front Filters ($\lambda_i = 266$ nm, Fig. 2), the heaviest detected mass varies from sample to sample: SP1_{FF} – m/z 400, SP2_{FF} – m/z 546, SP3_{FF} – m/z 546, and SP4_{FF} – m/z 522. The base peak is at m/z 202 for SP2_{FF}, SP3_{FF}, and SP4_{FF}, and at m/z 178 for SP1_{FF}. One can observe that the increase in oxidation air flow ($Q^{\text{air}}_{\text{SP3}} < Q^{\text{air}}_{\text{SP2}} < Q^{\text{air}}_{\text{SP4}} < Q^{\text{air}}_{\text{SP1}}$) results in a significant variation in the shape of the mass spectra. In the SP1 regime, most of the signal comes from three- and four-ring PAHs, while the heavier PAHs are less conspicuous. Regimes having the lowest oxidation air flow tend to produce more of the
245 heavier PAHs, although the increase of contribution for each mass is not the same. For samples SP2_{FF} and SP4_{FF} most of the



PAHs are concentrated in the mass range m/z 178–350 ($C_{14}H_{10}^+$ – $C_{28}H_{14}^+$), with comparable relative intensities. However, the SP3 regime has high peak intensities for $C_{14}H_{10}^+$ (m/z 178), $C_{16}H_{10}^+$ (m/z 202), $C_{18}H_{12}^+$ (m/z 228), and $C_{20}H_{12}^+$ (m/z 252), while the relative contributions of heavier PAHs remain comparable.



250 **Figure 2.** Comparison between mass spectra for SP1, SP2, SP3, and SP4 samples recorded with $\lambda_i = 266$ nm for Front Filters (lower spectra) and Back Filters (upper spectra). Note that four different areas have been averaged to yield each of these spectra. Proposed structural formulae based on molecular formulas obtained from mass spectra are also shown.

On Back Filters ($\lambda_i = 266$ nm, Fig. 2), the signal is mostly concentrated in a lower mass region than that of Front Filters. Mass spectra of all Back Filters are dominated by m/z 128 (naphthalene, $C_{10}H_8$). The spectrum of SP4_{BF} shows more peaks of higher masses than what is observed on other samples. The first aromatic compound visible on all samples is benzene (m/z 78), however its intensity is drastically reduced for both SP2_{BF} and SP3_{BF} compared to that of SP1_{BF} or SP4_{BF}. The same trend is observed for aromatic compounds lighter than m/z 128. Oxidation air flows associated with set points SP4 and SP1 thus resulted in the formation of more of the smallest-sized aromatic species (m/z 78–128).

260 Delhaye and coworkers showed that the total PAH signal in mass spectra obtained with $\lambda_i = 266$ nm can be indicative of the presence of organic carbon in aeronautical soot samples, because of the good agreement between total PAH mass signal and OC/TC values derived by a commonly-used thermo-optical protocol (see Fig. 7 in Delhaye et al., 2017). In Fig. 3, the total PAH signal, corresponding to the sum of all peaks attributed to PAHs in the 266 nm normalized mass spectra, is plotted against the oxidation air flow and is further compared to the OC/TC values given in Bescond et al. (2016) and Yon et al. (2015). According to these studies, SP1 has the lowest OC/TC ratio at 4.1 %, followed by SP4 (OC/TC 22.1 %), SP2



(OC/TC 46.8 %), and SP3 (OC/TC 87 %). Slightly different values for SP2 (OC/TC 58.3 %) and SP1 (OC/TC 16.2 %) are given by Yon et al. (2015), but the same overall trend is maintained. The same evolution with oxidation air flow was evidenced for the PAH to soot ratio in Moore et al. (2014) using a different method (photoelectric aerosol sensor). Figure 3 shows that the total PAH signal measured by mass spectrometry ($\lambda_i = 266$ nm) on Front Filters (orange bars) follows the same trend as the OC/TC ratios measured by the thermo-optical protocol for the same CAST set points (Bescond et al., 2016; Yon et al., 2015). Although the total PAH signal on Back Filters (blue bars, Fig. 3) also follows the trend observed on Front Filters for samples SP3_{BF}, SP2_{BF}, and SP4_{BF} (decreasing PAH signal with increasing oxidation air flow), total PAH signal of SP1_{BF} is high compared to that of SP1_{FF}. This is likely due to the nature of its PAH content, as discussed later on.

The total PAH signal derived from L2MS measurements ($\lambda_i = 266$ nm) can be further refined according to the PAH mass range distribution present on each sample (Fig. 3). The various CAST set points exhibit different PAH mass distributions on their Front and Back Filters, which likely relates to the different volatility properties of PAHs and probably affects their subsequent trapping on Front and Back Filters. Distinct volatility properties have been observed in the past on particles originating from wood combustion by Bari et al. (2010), who classified the PAHs on the basis of their number of aromatic rings resulting in the detection of three different PAHs categories. The authors classified the PAHs consisting of two aromatic rings as volatiles as they were mostly found in the gas phase, while those made of three and four rings were classified as semi-volatiles. PAHs comprising more than four rings were classified as non-volatile as they were observed in the PM in their study. Note that slightly different classes have also been defined in the literature (An et al., 2016; Elghawi et al., 2010; Sun et al., 2006). In our study, we largely found compounds consisting of one and two aromatic rings on Back Filters, while PAHs of m/z 176–242 were found on both Back and Front filters and those of $m/z \geq 252$ predominantly on Front Filters. Such PAH partitioning between Front and Back Filters is in line with the work of Bari et al. (2010). Similarly, we categorized the PAH distributions found on CAST samples into a volatile, semi-volatile, and non-volatile fraction (Fig. 3), where the volatile fraction encompasses here aromatic species made of one to two aromatic rings (m/z 78–166), the semi-volatile fraction comprises PAHs with a mass range of m/z 176–242, and the non-volatile fraction includes PAHs of $m/z \geq 252$.

The majority of PAHs were also detected with SPI at 157 nm for both Front and Back Filters, albeit at a lower signal intensity (as can be seen by comparing the two sets of spectra in Fig. 2 and Fig. S1). The overall shape changes due to the different ionization efficiencies of PAHs from R2PI at 266 nm to SPI at 157 nm. At lower masses, additional peaks with prominent features at m/z 28, 43, 55, 69 are present and are assigned to aliphatic fragment ions, which could result from multi-photon ionization processes. Analysis of the peak at m/z 31 suggests the presence of heteroatoms in the fragments as it cannot be assigned to a $C_nH_m^+$ hydrocarbon formula. The series m/z 91, 103, 115 corresponds to fragments ($C_7H_7^+$, $C_8H_7^+$, $C_9H_7^+$), which are attributed to alkylbenzene species (McLafferty and Tureček, 1993).

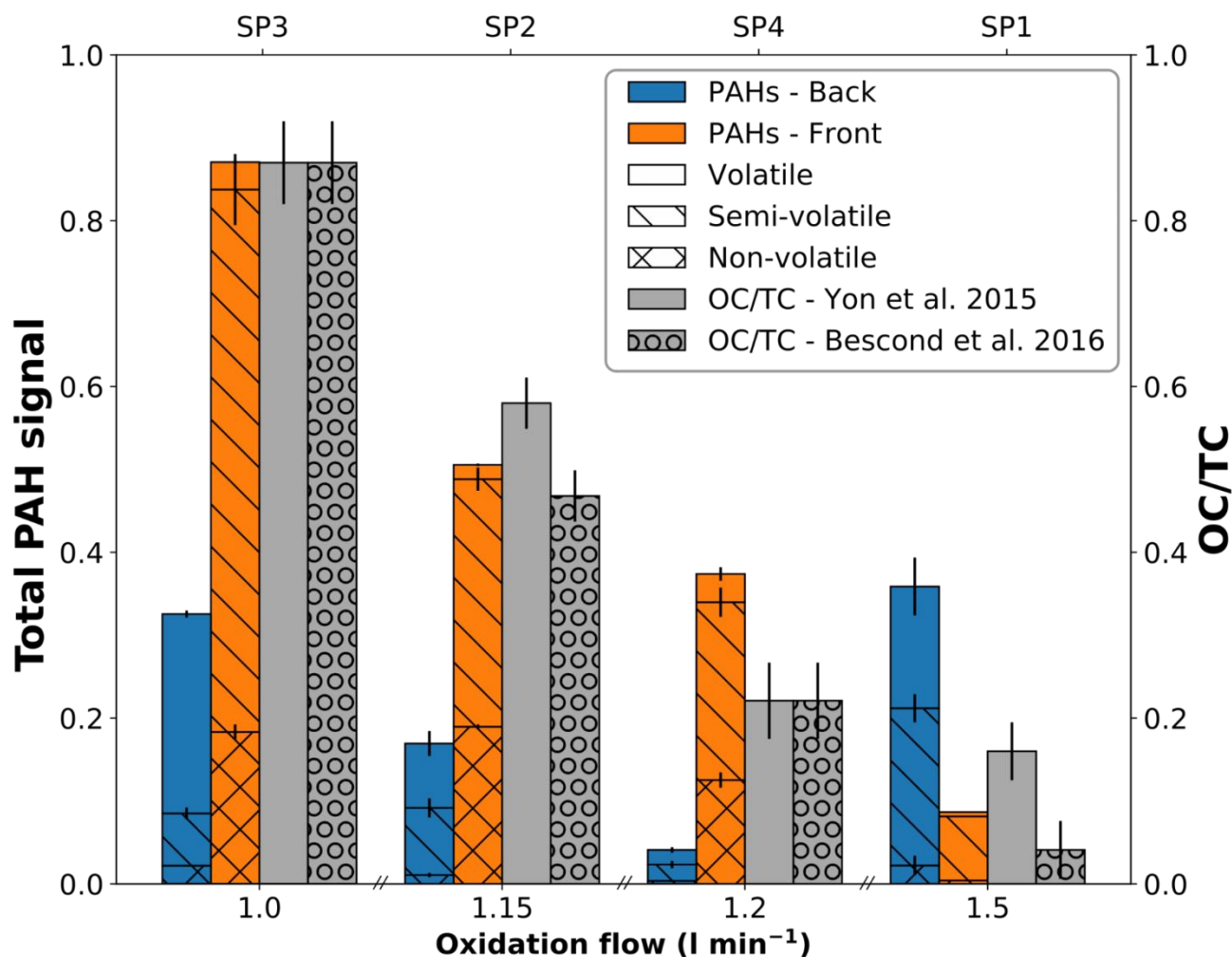


Figure 3. Variation in total PAH signal detected with L2MS at $\lambda_i = 266$ nm on Front (orange) and Back (blue) Filters plotted as a function of oxidation air flow. The PAH contribution is divided into adsorbed species (non-volatile, $m/z \geq 252$), semi-volatile (m/z 176–242), and volatile (m/z 78–166) fractions. OC/TC values reported in the literature are plotted in grey for comparison.

300

Mass spectra obtained with SPI at 118 nm (Fig. S1) show a high degree of fragmentation. In all cases, peaks at m/z 23 and 39 are due to the presence of trace amounts of usual contaminants Na and K. PAHs were detected on all samples, but the signal intensity is low due to a high fragmentation rate caused by the excess of energy at $\lambda_i = 118$ nm. Fragment ions at m/z 50, 51, 52, 53, 63, and 65 suggest also the presence of aromatic compounds. Series of highly unsaturated aliphatic compounds ($C_{2n}H_{2n}^+$ and $C_{2n}H_4^+$, $n = 2-5$) are present. Fragments of alkyl compounds ($C_nH_{2n+1}^+$) were also found at m/z 15, 29, 43, 57, 71, 85, and 99, with a relatively low intensity compared to fragments of aromatic compounds. Another distinctive series –

305



attributed to $C_nH_{2n}^+$ fragments – was found at m/z 28, 42, 56, and 70. These fragments may result from a McLafferty rearrangement involving alkene chains (McLafferty and Tureček, 1993).

310 3.1.2 Principal component analysis of L2MS spectra

In order to better discriminate the chemical composition of the various samples, particularly (i) the Front and Back Filters and (ii) the miniCAST set points, principal component analysis (PCA) was applied to mass spectra recorded for all three individual ionization wavelengths. A full description of this statistical method is provided in Sect. S2. Here, the covariance matrix was built from the integrated areas of all the detected peaks with a signal-to-noise ratio $SNR > 3$. The physical meaning of all derived principal components can be inferred from the contribution of the various molecular species to the loadings (see Sect. S2 and Fig. S2 and S3). By identifying the molecular families contributing to this variance, we can better interpret the PCA score plots (Fig. 4) and grasp the nature of the chemical differences between the samples.

315
320
325
330
335
340

In L2MS data generated with 266 nm ionization wavelength, the scree plot and loadings presented in Fig. S2a and S3a, respectively, show that PC1 expresses the largest variance (58.86 %) in the dataset and differentiates samples represented by a greater amount of high-mass PAHs (positive contribution: $m/z \geq 189$) from those containing more of low-mass PAHs and derivatives (negative contribution: up to three aromatic rings). PC2 (19.30 %) denotes the relative contribution between high-mass PAHs (positive contribution: $m/z \geq 216$) bearing four and more aromatic rings and aromatic compounds containing up to the mass of pyrene (m/z 202). The dataset, in terms of PC1 and PC2, is illustrated in a score plot in Fig. 4a. There is a notable separation between different samples which implies distinct chemical compositions of PM on the filters. The first conclusion is that, for all set points, PC1 is positive for Front Filters but negative for Back Filters, and therefore the main difference between Front and Back Filters can be defined as the greater amount of high-mass PAHs ($m/z \geq 189$) on Front Filters. The highest PC1 score is observed for SP2_{FF}, therefore it has the highest relative contribution from the high-mass PAHs, while SP3_{BF} (the most negative score of PC1) contains mostly light-weight aromatic species (≤ 3 aromatic rings). The PC1 score for Back Filters decreases along with the oxidation air flow indicating a greater contribution of aromatic species with 3 or less aromatic rings for lower oxidation air flows. Data points for Front Filters generally display a positive PC2 component except for SP1_{FF}, a phenomenon possibly explained by the small fraction of non-volatile PAHs produced in this regime.

In L2MS data generated with a 157 nm ionization wavelength, the scree plot and loadings displayed in Fig. S2b and S3b, respectively, show that PC1 (55.38 %) can be interpreted as the relative contribution of semi- and non-volatile PAHs and fragments (positive contribution) to fragments at m/z 25 and 26 and the very few volatile aromatic species (m/z 104, 128, 142, 152, 154, and 178, negative contribution), whereas PC2 (20.55 %) exhibits a positive contribution solely from semi-volatile species (m/z 176–242). Fig. 4b shows no clear separation between Front and Back Filters at this ionization wavelength. This is expected as the ionization energy (157 nm, 7.9 eV) is not enough to ionize naphthalene or its methyl derivatives, representative of the volatile compounds expected to be present in the gas phase (Bari et al., 2010). However, SP2_{FF} once again exhibits the highest PC1 score, meaning that its mass spectrum contains a large amount of semi- and non-

volatile species. $SP3_{FF}$ displays the highest PC2 score which translates into a high contribution from semi-volatile compounds. Low oxidation air flow conditions ($SP3$) result in the production of more semi-volatile compounds, while $SP2$ conditions generate a higher relative contribution from non-volatile compounds, resulting in more homogeneous mass spectra. While this ionization wavelength did not provide information on lightweight or volatile organic compounds, it yet confirmed the separation between semi and non-volatile compounds with CAST set points.

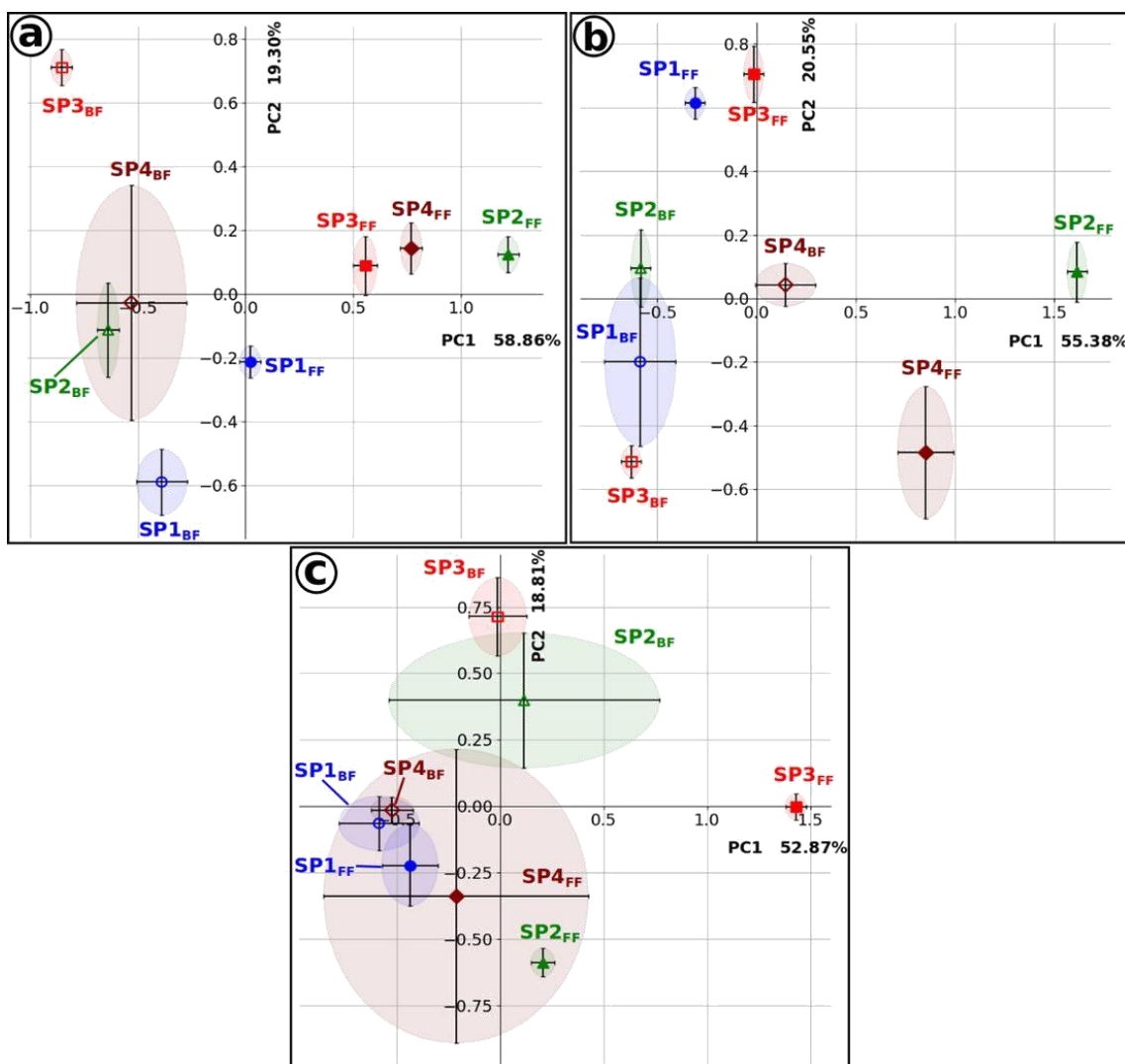


Figure 4. Score plots of PC2 vs PC1 derived from principal component analysis of the data obtained with 266 nm (a), 157 nm (b), and 118 nm (c) ionization.



In L2MS data generated with 118 nm ionization wavelength, the scree plot and loadings displayed in Fig. S2c and S3c, respectively, show that PC1 represents the contribution from aromatic compounds (m/z 178–252), while lower masses (m/z 50–98) largely influence PC2, and in particular $C_{2n}H_2^+$ and $C_{2n}H_4^+$. SP3_{FF} is the only sample with a relatively high contribution of aromatic compounds compared to low masses, resulting in a large PC1 score as seen in Fig. 4c. All other samples show a relatively low amount of aromatic species, and hence they do not diverge significantly in terms of PC1. Nevertheless, there is a clear trend in the aromatic contribution (AC), which increases ($AC_{SP1} < AC_{SP4} < AC_{SP2} < AC_{SP3}$) as the oxidation air flow decreases. SP2_{FF} contains the most $C_{2n}H_2^+$ and $C_{2n}H_4^+$, followed by SP4_{FF}. For the SP2 and SP3 regimes, it appears that $C_{2n}H_2^+$ and $C_{2n}H_4^+$ are mostly found on the PM, while for other working points the difference between their concentrations on Front and Back Filters is minimal.

3.2 SIMS analysis

3.2.1 Mass spectra obtained by SIMS

Spectra of SP1, SP2, SP3, and SP4 samples obtained with ToF-SIMS in positive mode are presented in Fig. 5 (m/z 150–500 range). All SIMS mass spectra feature a significant fragmentation, which is intrinsic to the technique and caused by the energetic primary ion beam. To start with Front Filter samples, and similarly to what has been observed in L2MS, the PAH distribution across samples varies with set points, the highest detected mass on SP1_{FF}, SP2_{FF}, SP3_{FF}, and SP4_{FF} being m/z 452, m/z 871, m/z 825, and m/z 908, respectively. Again, SP1_{FF} shows a shorter high-mass PAH “tail” compared to other Front Filter samples. The high-mass PAH region observed in SIMS is in good agreement with that of L2MS, whereas the significant fragmentation observed in SIMS seems to impair the low-mass region (ca. $m/z < 228$) more conspicuously and as a result makes SIMS and L2MS spectra look more distinct in this region. It is worth recalling also that SIMS measurements are performed at room temperature, which contrasts with L2MS measurements that involve nitrogen cooling. This may eventually result in SIMS analyses providing an incomplete picture for some specific low-mass PAHs (especially the volatile PM fraction), as further discussed below. The base peak of SP2_{FF}, SP3_{FF}, and SP4_{FF} samples is located at m/z 239 ($C_{19}H_{11}^+$), whereas SP1_{FF} exhibits its highest intensity peak at m/z 202 ($C_{16}H_{10}^+$). The absolute intensity of the overall signal is the highest for SP3_{FF}, followed by SP2_{FF}, SP4_{FF}, and SP1_{FF}. Likewise, the total PAH contribution in each sample (i.e. summed areas of all peaks attributed to PAHs in positive mode) decreases with the oxidation air flow rate for Front Filters, as shown in Fig. 6, which indicates that the general trend previously shown with L2MS is also observed with SIMS. Consequently, the total PAH signal derived from SIMS measurement is also in line with OC/TC measurements obtained from thermo-optical methods (Bescond et al., 2016; Yon et al., 2015) for all Front Filter samples (Fig. 6). Here, non-volatile species are predominant on SP3_{FF}, SP2_{FF}, and SP4_{FF}, while semi-volatiles constitute the main class of compounds observed on SP1_{FF}. The difference in which class of chemical compounds is predominant in L2MS and SIMS (Fig. 3 vs Fig. 6) is due to the ionization process ($\lambda_i = 266$ nm vs Bi_3^+ ion beam). Semi-volatile compounds (m/z 178–228) are predominant in spectra generated with 266 nm ionization wavelength, whereas high-mass aromatic compounds (m/z 250–500) dominate SIMS

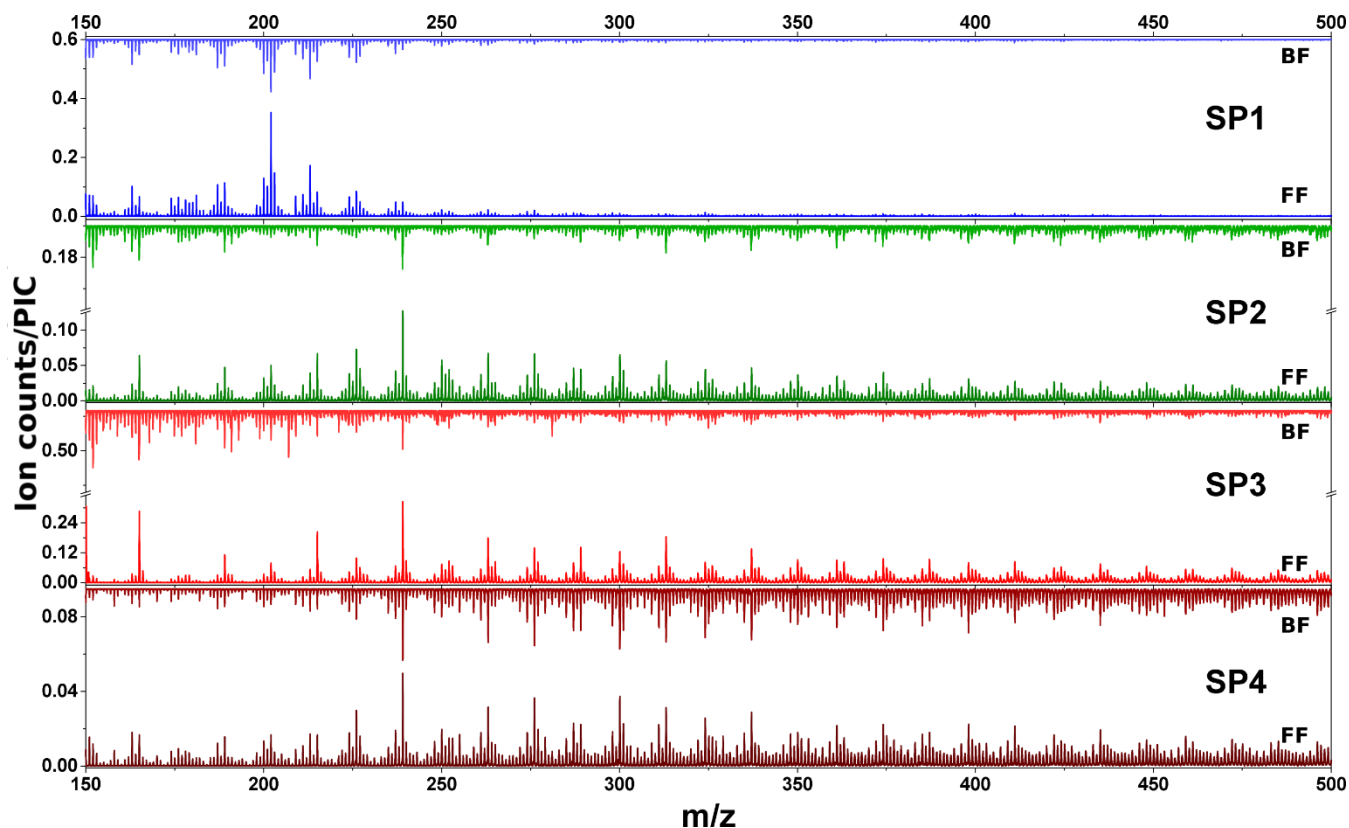


Figure 5. ToF-SIMS mass spectra of samples SP1, SP2, SP3, and SP4 obtained in positive polarity for Front Filters (lower spectra) and Back Filters (upper spectra). For visualization purposes, we focus on the m/z 150–500 range. Note that for SP2 and SP3 samples Front and Back filters have different scales.

mass spectra. This suggests that CAST samples contain PAHs with a high stability in the high-mass range (i.e. stabilomers, Stein and Fahr, 1985), which are eventually less prone to fragmentation in SIMS with respect to other semi-volatile compounds. Consequently, a smaller relative fraction of molecules is fragmented in L2MS which leads to a more reliable PAH content determination in the semi-volatile mass range from their L2MS mass spectra compared to SIMS.

As to the PAH distribution observed on Back Filters, it is distinct from that of Front Filters in that the highest mass detected is m/z 411 on SP1_{BF}, m/z 570 on SP2_{BF}, m/z 448 on SP3_{BF}, and m/z 793 on SP4_{BF} (i.e. the m/z distribution of Back Filters is less spread out towards high masses). The total PAH signal shows now a different behavior to that observed on Front Filters (Fig. 6), where SP4_{BF} exhibits the highest PAH signal, followed by SP2_{BF}, SP1_{BF}, and SP3_{BF}. Additionally, the PAH signal of SP4_{BF} determined by SIMS is higher than the one of its corresponding Front Filter, which is in contradiction to what has been derived from L2MS ($\lambda_i = 266$ nm) spectra, where the Front Filter showed a much higher PAH signal. This behavior



may originate from the nature of deposited PAH on Front and Back Filters, which may have different volatility and stability properties, as discussed above.

400

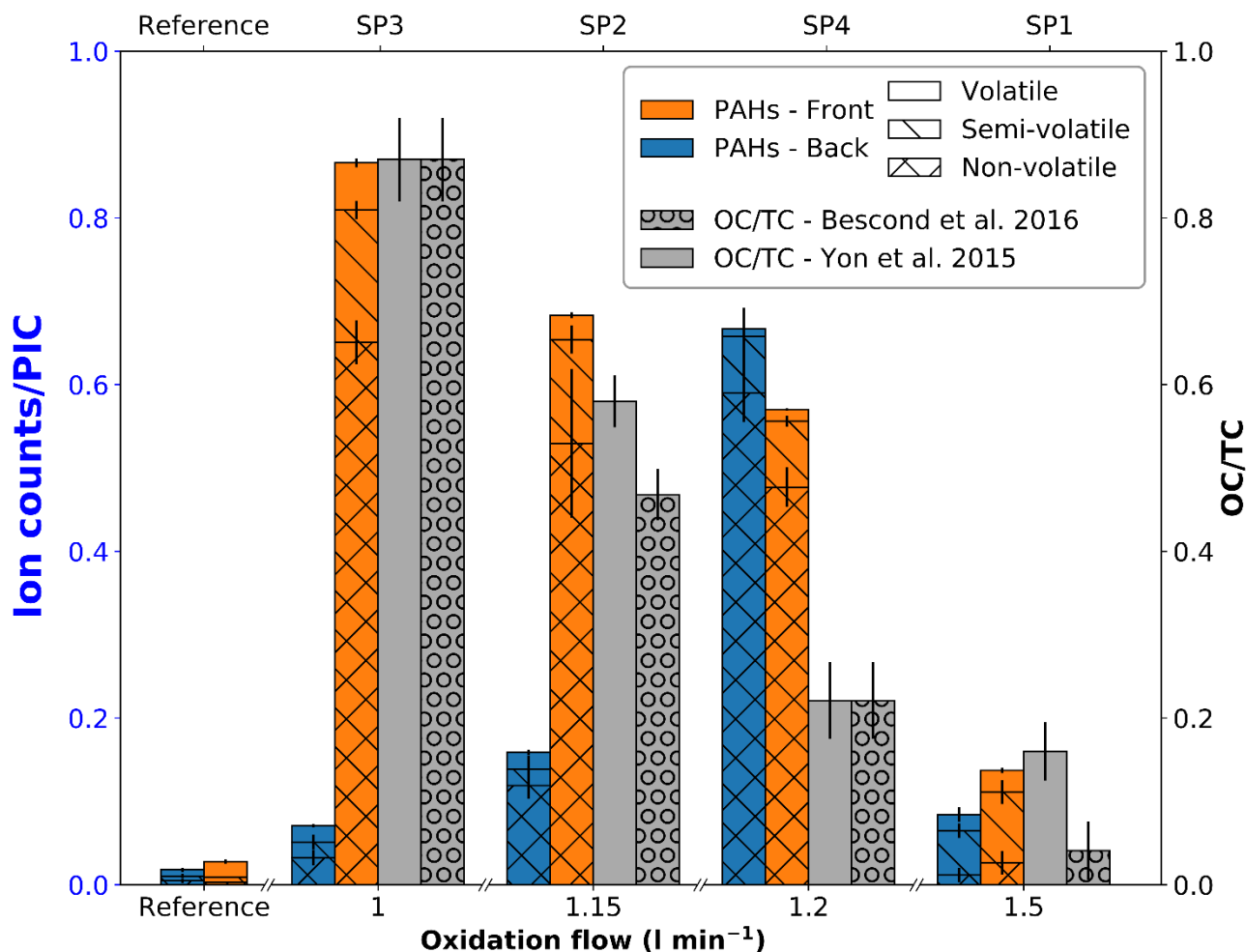


Figure 6. Total PAH signal detected with SIMS on Front (orange) and Back (blue) Filters plotted as a function of oxidation air flow, along with OC/TC values reported in the literature for the same CAST set points. All values are normalized to the partial ion count (PIC) corresponding to the signal of all selected peaks.

405

Negative polarity mass spectra obtained for Front and Back Filters are presented in Fig. S4. H⁻ and C₂⁻ fragment ions have the highest abundance in mass spectra of SP1_{FF} and SP1_{BF}, whereas SP2_{FF}, SP3_{FF}, SP4_{FF}, and SP4_{BF} are dominated by H⁻ and C₂H⁻. Similarly to that of the “reference” sample, spectra of SP2_{BF} and SP3_{BF} are dominated by H⁻ and OH⁻ ions. The C_nH⁻ series is observed in mass spectra of SP2, SP3, and SP4 samples (Front and Back Filters), with the intensity decreasing with



410 the mass (for $n \geq 2$). To further understand this behavior, the relative abundances of the C_n^- and C_nH^- fragments are plotted as
a function of the oxidation air flow in Fig. 7. C_n^- fragments are commonly considered as markers of the EC content (Duca et
al., 2019; Pagels et al., 2013; Popovicheva et al., 2017). For instance, Pagels et al. (2013) used the sum of C_n^- ($n = 2-4$)
fragment signals as a marker of EC in aerosol time-of-flight mass spectrometer (ATOFMS) measurements for wood stove
PM emissions and the same marker ions have been used to discriminate diesel from biodiesel PM emissions by Popovicheva
415 et al. (2017). C_nH^- fragments are commonly associated with OC contents (Ewinger et al., 1991; Le Roy et al., 2015), but it is
worth noticing that both series have been detected in mass spectra of pure PAHs (Bentz et al., 1995; Le Roy et al., 2015).
Here, the relative proportion of C_n^- fragments increases with the initial oxidation air flow conditions on Front Filter samples
and exhibits a similar contribution across Front and Back Filter samples. It should be noted also that the black carbon, pre-
deposited on Back Filters, contribute also to the C_n^- signal. However, for all CAST samples, the total C_n^- contribution is
420 higher than that of the “reference” sample, suggesting that some proportion of C_n^- on Back Filters originates from the
deposited material. On the other hand, the C_nH^- ion series shows a distribution across Front and Back samples akin to that of
the total PAH signal (i.e. the total PAH signal in positive polarity, see Fig. 6). This positive correlation indicates a possible
polyaromatic origin of the C_nH^- fragments. In order to better delineate the contributions of EC, PAHs, and other components
to the C_n^- carbon cluster series, Pearson correlation coefficients between all C_n^- and C_nH^- have been evaluated for the
425 complete set of negative SIMS spectra. C_n^- ($n = 1-4$) ions display high positive correlation ($r \geq 0.60$) with a maximal value
for C_3^- and C_4^- ($r = 0.91$). On the contrary, this group of peaks is not correlated with the C_5^- fragment ion and is
anticorrelated with all heavier carbon cluster ions ($n \geq 6$). This first analysis shows that at least two components contribute to
the C_n^- signal. Furthermore, positive correlations are also found between the C_nH^- ($n = 3-12$) fragments, but also between
these C_nH^- ions and the C_n^- ($n = 5-12$) fragments. For better visibility, specific subsets of C_n^- fragment ions ($n = 1-4$ and $n =$
430 $5-12$) are plotted separately in the lower panels of Fig. 7. The lower left panel shows that the ions with carbon numbers $n =$
 $1-4$ primarily contribute to the total C_n^- signal, whereas the lower right panel highlights the correlation between subset ions
with carbon numbers $n = 5-12$ and C_nH^- fragments. In addition, the similar distribution across Front and Back samples
between C_nH^- fragment ions and total PAH signal supports the fact that C_nH^- fragments can be considered as a marker for
OC (for which PAH are a proxy) in our soot samples. Therefore, while a predominant part of C_n^- fragments ($n = 1-4$) are
435 markers for EC, a non-negligible part (C_n^- with $n \geq 5$) also originates from the organic fraction present on our samples.

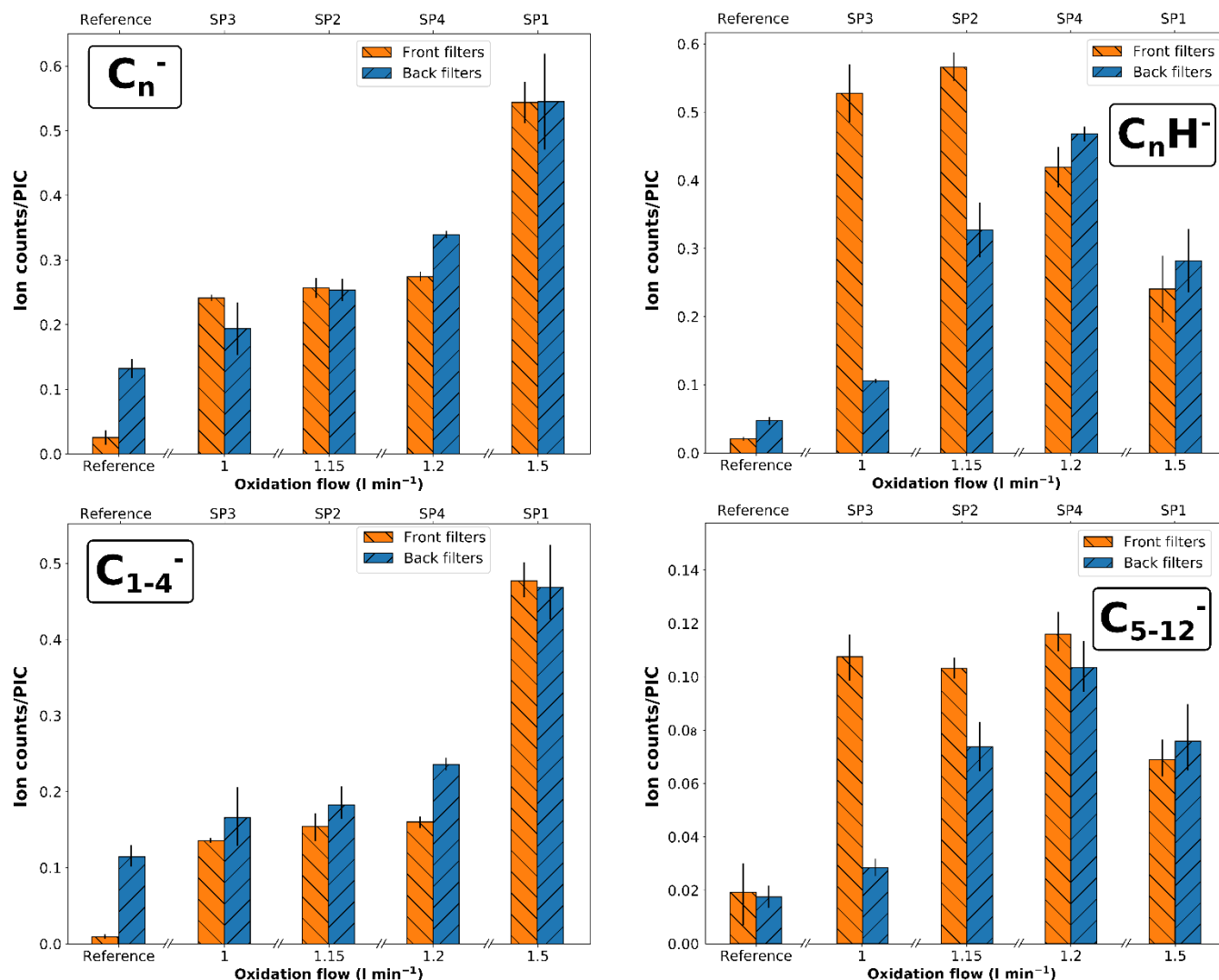


Figure 7. Variation of the signal of various markers, as derived from SIMS spectra. The panels represent the total peak areas of the following families: (upper left) total peak area of C_n^- , (upper right) total peak area of C_nH^- , (lower left) C_{1-4}^- , and (lower right) C_{5-12}^- . All values are normalized to the partial ion count (PIC) corresponding to the signal of all selected peaks.

440 3.2.2 Principal component analysis of SIMS spectra

PCA was applied to the positive mode SIMS spectra. All hydrocarbon fragments and the most representative peaks for PAHs were chosen for the analysis (see Sect. S3 and Fig. S4). The PCA score plot for the first two components (PC1 and PC2, responsible for 92 % of the variance) is presented in Fig. 8a, and their corresponding loadings in Fig. 8c. PC1 represents 73 % of the variance and is associated with fragment ions (positive coefficients), and with aromatic species with $m/z \geq 165$ (negative coefficients). All Back Filter samples (containing gas-phase PAHs) but SP4_{BF} have positive PC1 scores, whereas all Front Filters but SP1_{FF} exhibit negative PC1 scores due to their high PAH contents. SP1_{FF} and SP1_{BF} are located in almost

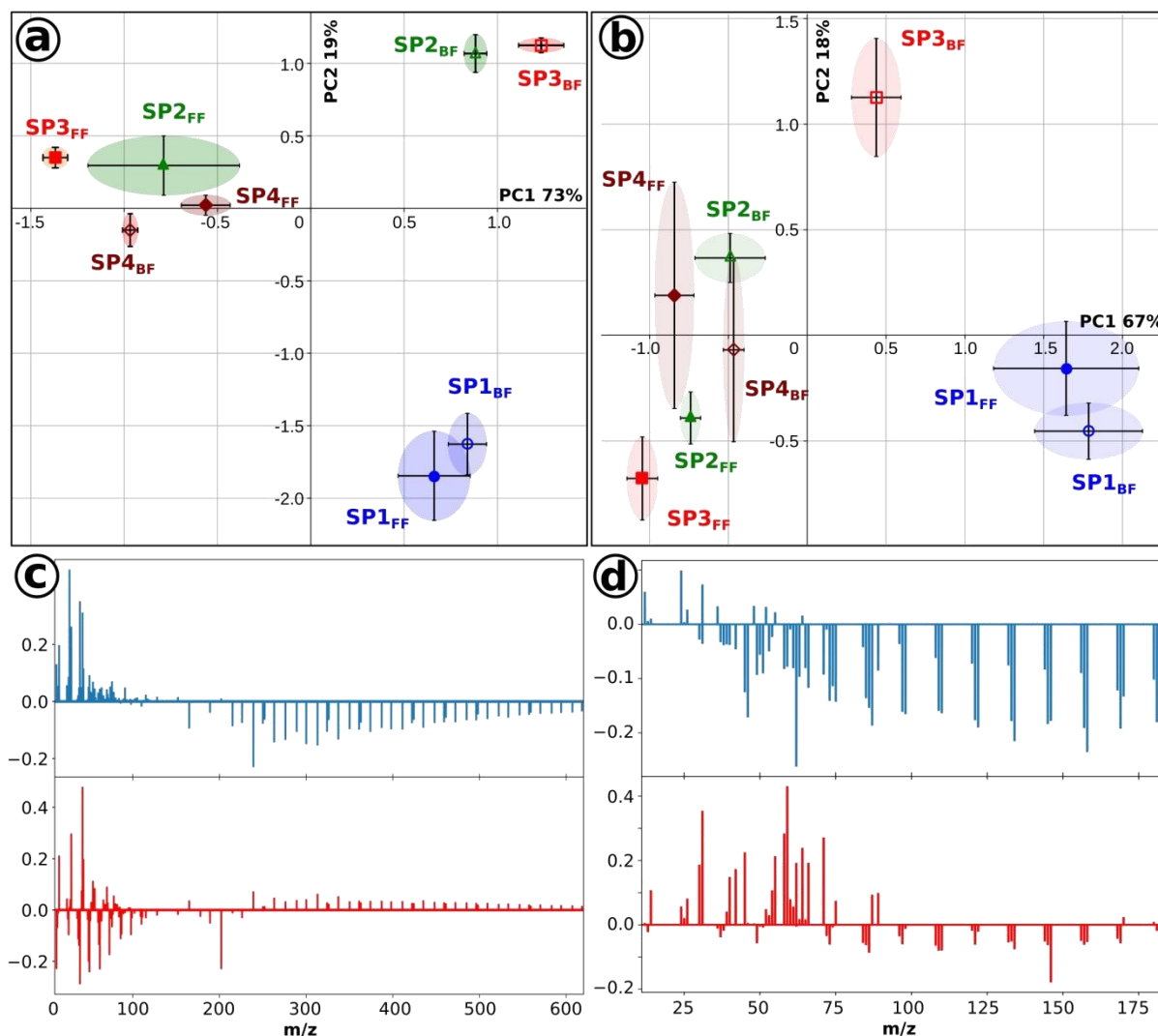
445



the same position due to their high scores on positive PC1 that corresponds to their low-mass PAH content. From this result, it can be determined that SP3_{FF} has the highest relative PAH content. Among front filters, SP1_{FF} has the smallest contribution from PAHs. SP3_{BF} has the highest contribution from fragments, associated with fragmentation of both aliphatic and aromatic species. The negative contribution of PC2 (19 % of the variance) is associated with the low-hydrogen content fragments ($C_nH_m^+$ with $m < n$) and semi-volatile PAHs (m/z 176–228). The positive coefficients of PC2 are associated with aliphatic fragments (e.g. $C_nH_m^+$ with $m > n$). As most of the variance was contained in only two principal components (92 %), there are only two available criteria for differentiating between samples: PC1, corresponding to the amount of PAHs, and PC2, depending partially to the hydrogen content of fragments originating from aromatic and aliphatic species. The strong fragmentation, intrinsic to the SIMS method, is a limitation to this type of analysis. In this case, we are not able to fully differentiate between fragments coming from species with different volatility which could explain why SP4_{BF} exhibits a negative PC1 score. Nevertheless, there is a notable separation between data coming from different samples, with the exception of SP1 (for the previously discussed reasons). However, there is no visible grouping for the Back/Front Filters or for the different working points. PCA was also applied to the negative mode SIMS spectra for selected mass peaks, including carbon clusters C_n^- , organic content markers C_nH^- , and some oxygenated and nitrogenated fragment ions. The first two components were determined to represent more than 85 % of the variance. The score plot of PC1 vs PC2 is presented in Fig. 8b, along with their corresponding loadings (Fig. 8d). The first component, which accounts for over 67 % of the variance, separates the samples containing low-mass carbon clusters C_n^- (with $n < 3$), nitrogen and oxygen bearing compounds (e.g. CN^- , HNO_3^- , C_3O^-) (positive PC1) from the samples containing species with a higher mass (hydrocarbons, oxygenated, and nitrogenated fragments – negative contribution). PC2, accounting for 18 % of the variance, separates data points based on the contribution from hydrocarbon compounds ($C_nH_m^-$, negative PC2) and oxygen/nitrogen bearing fragments (positive contribution). It is worth noting that SP4_{FF} is the only front filter with a positive PC2 value, having a much more important contribution from oxygenated and nitrogenated compounds.

3.3 Raman micro-spectroscopy analysis

Raman spectra measured for each sample are presented in Fig. 9. All spectra for PM deposited on Front Filters are in very good agreement with those already measured for the same miniCAST set points (e.g. Ess et al., 2016), while the spectra of PM on Back Filters are dominated by the absorption of the pre-deposited black carbon. Soot particles often exhibit distinct Raman signatures that can be used to distinguish samples mostly by their hybridization and nanostructure (e.g. stacking properties) compared to that obtained for a perfect graphite crystal, i.e. a crystal made of sp^2 -hybridized carbons and graphene sheets stacked with their surfaces parallel and slightly offset. When samples differ from perfect crystalline graphite, defects appear and can take the form of stacking disorder (such as in turbostratic arrangements where tortuosity reduces the stacking order), edge sites, missing atoms in the graphite lattice or even altered local or semi-long range arrangements of carbon atoms (Parent et al., 2016).

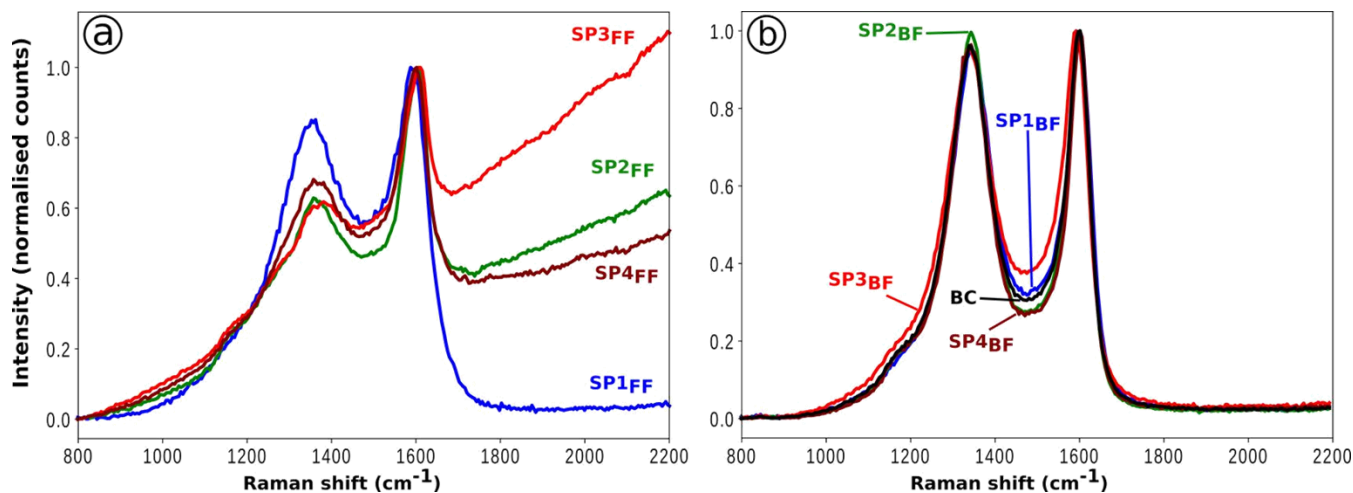


480 **Figure 8.** Score plots of PC1 and PC2 derived from positive (a) and negative (b) polarity SIMS mass spectra of CAST soot
 485 samples SP1, SP2, SP3, and SP4 (Front and Back Filters). Loadings corresponding to the contribution of different species to
 PC1 (blue line) and PC2 (red line) derived from positive (c) and negative (d) polarity SIMS mass spectra.

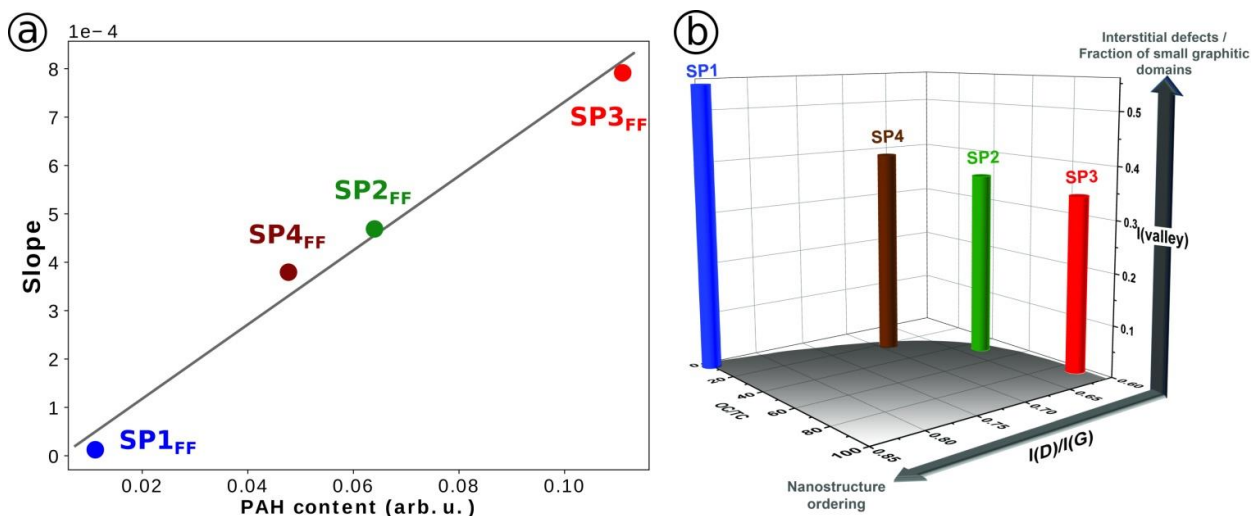
Both the underlying fluorescence and the soot Raman feature are observed to vary significantly with the set point (Fig. 9).
 485 The former refers to the baseline, whereas the latter refers to the two broad bands centered at 1356 cm^{-1} and 1598 cm^{-1} ,
 termed D (for defect) and G (for graphite), which correspond to Raman scattering involving E_{2g} and A'_{1g} symmetry,
 respectively (Ferrari and Robertson, 2000; Sadezky et al., 2005). The fluorescence background (SP3 > SP2 > SP4 > SP1),
 attributed to surface organic content (Cloutis et al., 2016), is observed to decrease with increasing oxidation air flow for
 Front Filter samples. This trend is even clearer when the fluorescence slope fitted as a straight line between 800 and 2200 cm^{-1}



490 (Raman shift) is plotted against the PAH signal determined in L2MS (Fig. 10). The linear fit ($R^2 = 0.992$) obtained in Fig. 10 reflects the good agreement between the fluorescence background and the measured trend in total PAH signal. For Back Filter samples, the fluorescence background signal is nonexistent and spectra resemble that of black carbon except in the “valley” region (i.e. in between the two soot peaks).



495 **Figure 9.** Raman spectra of SP1 (blue), SP2 (green), SP3 (red), and SP4 (brown) samples on Front Filter (a) and Back Filter (b). For all samples, plots are normalized to the maximum intensity of the G band. The spectrum of pure black carbon (BC) deposited on a QFF is plotted in black in panel (b) for comparison.



500 **Figure 10.** (a) Fluorescence slopes extracted from Raman spectra of SP1F F - (blue), SP2F F (green), SP3F F (red), and SP4F F (brown) plotted against total PAH content measured in L2MS (in terms of ion signal) in Front Filter samples, (b) 3-D bar plot showing the evolution of the intensity of the “valley” between the two D and G bands and that of the I(D)/I(G) height-ratio with organic content (OC/TC ratio) in Front Filter samples.



Two conclusions can be drawn from these observations. First, when comparing fluorescence signals of Back and Front Filter samples to PAH content, we can further refine our definition of organic content. Fluorescence is not just related to the total PAH signal, although this is a good marker of organic content. If it were, fluorescence would also be observed for Back Filter samples, in accordance with their relatively high gas-phase PAH contents. The lack of fluorescence signal on Back Filters, whose chemical composition is dominated by small PAHs, suggests that the fluorescence can be attributed mainly to non-volatile PAHs in the particulate phase, even though the heaviest mass detected in L2MS (m/z 546) is still small to expect fluorescence with a 514 nm excitation wavelength (Mercier et al., 2019). Consequently, the interaction of PAHs with one another or with the PM surface seems to trigger the fluorescence excited at 514 nm. Such perturbative effect (e.g. aggregate formation) on the luminescence has been observed in solutions (Nakagawa et al., 2013).

Information on soot nanostructure ordering can be derived from the I(D)/I(G) height-ratio, whose increase in intensity reflects a higher degree of order for soot made of crystallites (L_c) smaller than 2 nm (Ess et al., 2016; Ferrari and Robertson, 2000). The height (intensity) of the valley region between the two peaks (1440–1540 cm^{-1}) provides insights into the presence of interstitial defects which may distort the lattice structure (Ess et al., 2016; Ferrari and Robertson, 2000; Sadezky et al., 2005) or into the occurrence of small graphitic domains (Parent et al., 2016). For comparison purposes, Raman spectra measured for Front Filters (Fig. 10a) have been subsequently baseline-subtracted and normalized to the G band before interpretation. Figure 10b shows the evolution of the I(D)/I(G) height-ratio and that of the intensity of the “valley” region with the OC/TC ratio for each set point. This 3D-bar plot confirms that the nanostructure order (I(D)/I(G) height-ratio) increases with decreasing OC content, i.e. the degree of order in the large polyaromatic network is higher under SP1 conditions (i.e. at higher oxidation air flow). This is in agreement with the analysis of Ess et al. (2016) of soot produced at set points SP1, SP2, and SP3. Furthermore, a similar behavior with the oxidation air flow has been observed through an analogous Raman tracer ($AD1/(AG+AD2)$) involving the integrated band areas (Carpentier et al., 2012), from soot consisting of polyaromatic units poorly linked together (analogous to SP3_{FF}) to soot made of cross-linked structures with aliphatic bridges (analogous to SP1_{FF}). Figure 10b shows that SP1 working point produces soot composed of a larger polyaromatic network (larger crystallite size) and a greater fraction of small interconnected graphitic domains (high “valley” intensity) compared to SP3_{FF}. These results are in line with what has been previously observed for such CAST soot particles (Ouf et al., 2016), where the SP3 set point produced particles with very small crystallites (0.6 nm) and the greatest tortuosity/disordered structure (HRTEM) among all CAST samples.

530 4 Conclusions

Combustion by-products (PM and gas-phase) produced by a miniCAST generator are first separated and then characterized using a two-filter collection method and a multi-technique analytical/statistical protocol. Front and Back Filters thus generated are representative of the exhaust stream and are subsequently analyzed through first, an original L2MS technique featuring 3 ionization schemes, followed by SIMS, and last micro-Raman spectroscopy. An original three-wavelength L2MS scheme is employed in our study to target specific classes of compounds. On the one hand, we evidence the presence of



aliphatic compounds and specific fragment ions (118 nm), and on the other hand, we can focus on aromatic species (266 nm). Aromatic species were detected in all mass spectra (L2MS and SIMS). When combined with advanced statistical methods (PCA), mass spectrometry datasets revealed how different all samples were. Based on the PAHs classification of Bari et al. (2010), we were able to discuss aromatics distribution across Front and Back Filters in terms of volatile (1–2 rings), semi-volatile (3–4 rings), and non-volatile PAHs (larger than 4 rings). We determined that PM is essentially sampled on Front Filters, whereas the dominant compounds trapped on all Back Filters are volatile PAHs regardless of the combustion conditions. The good separation between the two phases confirms the high particle collection capability of QFF Front Filters. PCA revealed that distinct amounts of volatile compounds were present in samples produced with different combustion parameters. Specifically, changes in oxidation air flow conditions in the miniCAST resulted in notable changes in the mass distribution for both Front and Back Filters. L2MS results at 266 nm indicated that low oxidation air flow conditions (SP2 and SP3) produced more semi-volatile and non-volatile compounds in the exhaust stream. The addition of quenching gas (N₂) in the miniCAST combustion conditions (SP4) lessened the difference between Front and Back Filters which featured more homogeneous mass spectra. Complementary micro-Raman spectroscopy analyses not only confirmed the relationship between the underlying fluorescence and the total PAH signal determined by mass spectrometry, but also identified as non-volatile the nature of PAHs involved in the fluorescence and detected in the particulate phase. Finally, all analyses confirmed the validity of total PAH signal as a proxy for the organic content (OC) commonly detected in thermo-optical measurements (Bescond et al., 2016; Yon et al., 2015). Accordingly, the total PAH signal measured by mass spectrometry was observed to decrease with increasing oxidation air flow conditions in the miniCAST. The two-filter collection method in conjunction with our multi-technique analytical/statistical protocol brings us closer to in-situ measurements, as the predominant chemical properties of the particles deposited on filters are preserved and can be directly compared to those determined by in-situ techniques (e.g. Ouf et al., 2016).

Data availability. The data presented here can be provided on request to the contact author.

Supplement link (will be included by Copernicus)

Author contribution. YC, CP, AF, CI, and CF conceptualized and built the sampling system and defined the methodology; LDN, YC, RI, CI, GL, and CP performed the sample collection; LDN (SIMS), DD and MV (L2MS), RI, JAN and CP (Raman) performed the analysis and data reduction; LDN, YC, DD, MV, JAN, CP, and CF interpreted the results and wrote the original draft with additional contributions from other co-authors: IKO, AF, CI, MZ, and BC. JY, ET, CI, YC and CF provided funding and access to experimental infrastructure and organized the sampling campaign. All co-authors reviewed and approved the manuscript.

Competing interests. The authors declare that they have no conflict of interest.



Acknowledgements. This work was supported by the French National Research Agency (ANR) through the PIA (Programme d'Investissement d'Avenir) under contract ANR-10-LABX-005 (CaPPA – Chemical and Physical Properties of the Atmosphere), the European Commission Horizon 2020 project PEMS4Nano (H2020 Grant Agreement #724145), and the CLIMIBIO project via the Contrat de Plan Etat-Région of the Hauts-de-France region. J.A.N. acknowledges the financial support of Horiba Scientific. The measurement campaign was financed by GDR Suie (GDR CNRS 3622).

References

An, Y. Z., Teng, S. P., Pei, Y. Q., Qin, J., Li, X. and Zhao, H.: An experimental study of polycyclic aromatic hydrocarbons and soot emissions from a GDI engine fueled with commercial gasoline, *Fuel*, 164, 160–171, doi:10.1016/j.fuel.2015.10.007, 2016.

Atkinson, R. and Arey, J.: Atmospheric chemistry of gas-phase polycyclic aromatic hydrocarbons: formation of atmospheric mutagens., *Environ. Health Perspect.*, 102(suppl 4), 117–126, doi:10.1289/ehp.94102s4117, 1994.

Bandowe, B. A. M., Meusel, H., Huang, R., Ho, K., Cao, J., Hoffmann, T. and Wilcke, W.: PM_{2.5}-bound oxygenated PAHs, nitro-PAHs and parent-PAHs from the atmosphere of a Chinese megacity: Seasonal variation, sources and cancer risk assessment, *Sci. Total Environ.*, 473–474, 77–87, doi:10.1016/J.SCITOTENV.2013.11.108, 2014.

Bari, M. A., Baumbach, G., Kuch, B. and Scheffknecht, G.: Particle-phase concentrations of polycyclic aromatic hydrocarbons in ambient air of rural residential areas in southern Germany, *Air Qual. Atmos. Heal.*, 3(2), 103–116, doi:10.1007/s11869-009-0057-8, 2010.

Bentz, J. W. G., Goschnick, J., Schuricht, J. and Ache, H. J.: Depth-resolved investigation of the element and compound inventory of aerosol particles from outdoor air, *Fresenius. J. Anal. Chem.*, 353(5–8), 559–564, doi:10.1007/BF00321323, 1995.

Bescond, A., Yon, J., Ouf, F. X., Ferry, D., Delhaye, D., Gaffié, D., Coppalle, A. and Rozé, C.: Automated Determination of Aggregate Primary Particle Size Distribution by TEM Image Analysis: Application to Soot, *Aerosol Sci. Technol.*, 48(8), 831–841, doi:10.1080/02786826.2014.932896, 2014.

Bescond, A., Yon, J., Ouf, F.-X., Rozé, C., Coppalle, A., Parent, P., Ferry, D. and Laffon, C.: Soot optical properties determined by analyzing extinction spectra in the visible near-UV: Toward an optical speciation according to constituents and structure, *J. Aerosol Sci.*, 101, 118–132, doi:10.1016/J.JAEROSCI.2016.08.001, 2016.

Brochot, C., Abdolghader, P., Haghghat, F. and Bahloul, A.: Filtration of nanoparticles applied in general ventilation, *Sci. Technol. Built Environ.*, 25(2), 114–127, doi:10.1080/23744731.2018.1500396, 2019.

Butcher, D. J.: Vacuum Ultraviolet Radiation for Single-Photoionization Mass Spectrometry: A Review, *Microchem. J.*, 62(3), 354–362, doi:10.1006/MCHJ.1999.1745, 1999.



- Carpentier, Y., Féraud, G., Dartois, E., Brunetto, R., Charon, E., Cao, A.-T., D'Hendecourt, L., Bréchignac, P., Rouzaud, J.-N. and Pino, T.: Nanostructuring of carbonaceous dust as seen through the positions of the 6.2 and 7.7 μm AIBs, *Astron. Astrophys.*, 548, A40, doi:10.1051/0004-6361/201118700, 2012.
- 600 Chazallon, B., Ziskind, M., Carpentier, Y. and Focsa, C.: CO₂ Capture using semi-clathrates of quaternary ammonium salt: Structure change induced by CO₂ and N₂ enclathration, *J. Phys. Chem. B*, 118(47), 13440–13452, doi:10.1021/jp507789z, 2014.
- Cloutis, E., Szymanski, P., Applin, D. and Goltz, D.: Identification and discrimination of polycyclic aromatic hydrocarbons using Raman spectroscopy, *Icarus*, 274, 211–230, doi:10.1016/J.ICARUS.2016.03.023, 2016.
- 605 Dachs, J. and Eisenreich, S. J.: Adsorption onto aerosol soot carbon dominates gas-particle partitioning of polycyclic aromatic hydrocarbons, *Environ. Sci. Technol.*, 34(17), 3690–3697, doi:10.1021/es991201+, 2000.
- Delhaye, D., Ouf, F.-X., Ferry, D., Ortega, I. K., Penanhoat, O., Peillon, S., Salm, F., Vancassel, X., Focsa, C., Irimiea, C., Harivel, N., Perez, B., Quinton, E., Yon, J. and Gaffie, D.: The MERMOSE project: Characterization of particulate matter emissions of a commercial aircraft engine, *J. Aerosol Sci.*, 105, 48–63, doi:10.1016/J.JAEROSCI.2016.11.018, 2017.
- 610 Duca, D., Irimiea, C., Faccineto, A., Noble, J. A., Vojkovic, M., Carpentier, Y., Ortega, I. K., Pirim, C. and Focsa, C.: On the benefits of using multivariate analysis in mass spectrometric studies of combustion-generated aerosols, *Faraday Discuss.*, doi:10.1039/C8FD00238J, 2019.
- Elghawi, U. M., Mayouf, A., Tsolakis, A. and Wyszynski, M. L.: Vapour-phase and particulate-bound PAHs profile generated by a (SI/HCCI) engine from a winter grade commercial gasoline fuel, *Fuel*, 89(8), 2019–2025, doi:10.1016/J.FUEL.2010.01.002, 2010.
- 615 Ess, M. N., Ferry, D., Kireeva, E. D., Niessner, R., Ouf, F. X. and Ivleva, N. P.: In situ Raman microspectroscopic analysis of soot samples with different organic carbon content: Structural changes during heating, *Carbon*, 105, 572–585, doi:10.1016/j.carbon.2016.04.056, 2016.
- Ewinger, H.-P., Goschnick, J. and Ache, H. J.: Analysis of organic compounds with SNMS, *Fresenius. J. Anal. Chem.*, 341(1–2), 17–19, doi:10.1007/BF00322099, 1991.
- 620 Faccineto, A., Thomson, K., Ziskind, M. and Focsa, C.: Coupling of desorption and photoionization processes in two-step laser mass spectrometry of polycyclic aromatic hydrocarbons, *Appl. Phys. A Mater. Sci. Process.*, 92(4), 969–974, doi:10.1007/s00339-008-4605-0, 2008.
- 625 Faccineto, A., Desgroux, P., Ziskind, M., Therssen, E. and Focsa, C.: High-sensitivity detection of polycyclic aromatic hydrocarbons adsorbed onto soot particles using laser desorption/laser ionization/time-of-flight mass spectrometry: An approach to studying the soot inception process in low-pressure flames, *Combust. Flame*, 158(2), 227–239,



doi:10.1016/j.combustflame.2010.08.012, 2011.

Faccinnetto, A., Focsa, C., Desgroux, P. and Ziskind, M.: Progress toward the Quantitative Analysis of PAHs Adsorbed on Soot by Laser Desorption/Laser Ionization/Time-of-Flight Mass Spectrometry, *Environ. Sci. Technol.*, 49(17), 10510–10520, doi:10.1021/acs.est.5b02703, 2015.

630 Ferge, T., Karg, E., Schröppel, A., Coffee, K. R., Tobias, H. J., Frank, M., Gard, E. E. and Zimmermann, R.: Fast Determination of the Relative Elemental and Organic Carbon Content of Aerosol Samples by On-Line Single-Particle Aerosol Time-of-Flight Mass Spectrometry, *Environ. Sci. Technol.*, 40(10), 3327–3335, doi:10.1021/es050799k, 2006.

Ferrari, A. and Robertson, J.: Interpretation of Raman spectra of disordered and amorphous carbon, *Phys. Rev. B - Condens. Matter Mater. Phys.*, 61(20), 14095–14107, doi:10.1103/PhysRevB.61.14095, 2000.

635 Hilbig, R.: Narrowband tunable VUV radiation generated by nonresonant sum-and difference-frequency mixing in xenon and krypton, *Appl. Opt.*, 21(5), 913–917, doi:10.1364/AO.21.000913, 1982.

Irimiea, C., Faccinnetto, A., Carpentier, Y., Ortega, I. K., Nuns, N., Therssen, E., Desgroux, P. and Focsa, C.: A comprehensive protocol for chemical analysis of flame combustion emissions by secondary ion mass spectrometry, *Rapid Commun. Mass Spectrom.*, 32(13), 1015–1025, doi:10.1002/rcm.8133, 2018.

640 Irimiea, C., Faccinnetto, A., Mercier, X., Ortega, I.-K., Nuns, N., Therssen, E., Desgroux, P. and Focsa, C.: Unveiling trends in soot nucleation and growth: When secondary ion mass spectrometry meets statistical analysis, *Carbon*, 144, 815–830, doi:10.1016/J.CARBON.2018.12.015, 2019.

Kim, K.-H., Jahan, S. A., Kabir, E. and Brown, R. J. C.: A review of airborne polycyclic aromatic hydrocarbons (PAHs) and their human health effects, *Environ. Int.*, 60, 71–80, doi:10.1016/J.ENVINT.2013.07.019, 2013.

645 Lindsley, W. G.: Filter Pore Size and Aerosol Sample Collection, in *NIOSH Manual of Analytical Methods (NMAM)*, 5th Edition, p. FP 1-14. [online] Available from: <https://www.cdc.gov/niosh/docs/2014-151/pdfs/chapters/chapter-fp.pdf>, 2016.

McLafferty, F. W. and Tureček, F.: *Interpretation of mass spectra*, University Science Books., 1993.

650 Mercier, X., Carrivain, O., Irimiea, C., Faccinnetto, A. and Therssen, E.: Dimers of polycyclic aromatic hydrocarbons: the missing pieces in the soot formation process, *Phys. Chem. Chem. Phys.*, 21(16), 8282–8294, doi:10.1039/C9CP00394K, 2019.

Mihesan, C., Ziskind, M., Therssen, E., Desgroux, P. and Focsa, C.: IR laser resonant desorption of polycyclic aromatic hydrocarbons, *Chem. Phys. Lett.*, 423(4–6), 407–412, doi:10.1016/J.CPLETT.2006.04.032, 2006.

Mihesan, C., Ziskind, M., Therssen, E., Desgroux, P. and Focsa, C.: Parametric study of polycyclic aromatic hydrocarbon laser desorption, *J. Phys. Condens. Matter*, 20(2), 025221, doi:10.1088/0953-8984/20/02/025221, 2008.



- 655 Moldanová, J., Fridell, E., Popovicheva, O., Demirdjian, B., Tishkova, V., Faccinnetto, A. and Focsa, C.: Characterisation of particulate matter and gaseous emissions from a large ship diesel engine, *Atmos. Environ.*, 43(16), 2632–2641, doi:10.1016/J.ATMOSENV.2009.02.008, 2009.
- Moore, R. H., Ziemba, L. D., Dutcher, D., Beyersdorf, A. J., Chan, K., Crumeyrolle, S., Raymond, T. M., Thornhill, K. L., Winstead, E. L. and Anderson, B. E.: Mapping the operation of the miniature combustion aerosol standard (Mini-CAST) soot generator, *Aerosol Sci. Technol.*, 48(5), 467–479, doi:10.1080/02786826.2014.890694, 2014.
- 660 Mueller, L., Jakobi, G., Orasche, J., Karg, E., Sklorz, M., Abbaszade, G., Weggler, B., Jing, L., Schnelle-Kreis, J. and Zimmermann, R.: Online determination of polycyclic aromatic hydrocarbon formation from a flame soot generator *Aerosols and Health, Anal. Bioanal. Chem.*, 407(20), 5911–5922, doi:10.1007/s00216-015-8549-x, 2015.
- Nakagawa, K., Numata, Y., Ishino, H., Tanaka, D., Kobayashi, T. and Tokunaga, E.: Excimer luminescence from nonresonantly excited pyrene and perylene molecules in solution, *J. Phys. Chem. A*, 117(45), 11449–11455, doi:10.1021/jp402330n, 2013.
- 665 Nisbet, I. T. . and LaGoy, P. K.: Toxic equivalency factors (TEFs) for polycyclic aromatic hydrocarbons (PAHs), *Regulatory Toxicology and Pharmacology, Regul. Toxicol. Pharmacol.*, 16, 290–300, 1992.
- Ouf, F. X., Parent, P., Laffon, C., Marhaba, I., Ferry, D., Marcillaud, B., Antonsson, E., Benkoula, S., Liu, X. J., Nicolas, C., Robert, E., Patanen, M., Barreda, F. A., Sublemontier, O., Coppalle, A., Yon, J., Miserque, F., Mostefaoui, T., Regier, T. Z., Mitchell, J. B. A. and Miron, C.: First in-flight synchrotron X-ray absorption and photoemission study of carbon soot nanoparticles, *Sci. Rep.*, 6, doi:10.1038/srep36495, 2016.
- 670 Pagels, J., Dutcher, D. D., Stolzenburg, M. R., McMurry, P. H., Gälli, M. E. and Gross, D. S.: Fine-particle emissions from solid biofuel combustion studied with single-particle mass spectrometry: Identification of markers for organics, soot, and ash components, *J. Geophys. Res. Atmos.*, 118(2), 859–870, doi:10.1029/2012JD018389, 2013.
- 675 Pandey, S. K., Kim, K. H. and Brown, R. J. C.: A review of techniques for the determination of polycyclic aromatic hydrocarbons in air, *TrAC - Trends Anal. Chem.*, 30(11), 1716–1739, doi:10.1016/j.trac.2011.06.017, 2011.
- Parent, P., Laffon, C., Marhaba, I., Ferry, D., Regier, T. Z., Ortega, I. K., Chazallon, B., Carpentier, Y. and Focsa, C.: Nanoscale characterization of aircraft soot: A high-resolution transmission electron microscopy, Raman spectroscopy, X-ray photoelectron and near-edge X-ray absorption spectroscopy study, *Carbon N. Y.*, 101, 86–100, doi:10.1016/j.carbon.2016.01.040, 2016.
- 680 Popovicheva, O. B., Irimiea, C., Carpentier, Y., Ortega, I. K., Kireeva, E. D., Shonija, N. K., Schwarz, J., Vojtíšek-Lom, M. and Focsa, C.: Chemical composition of diesel/biodiesel particulate exhaust by FTIR spectroscopy and mass spectrometry: Impact of fuel and driving cycle, *Aerosol Air Qual. Res.*, 17(7), 1717–1734, doi:10.4209/aaqr.2017.04.0127, 2017.



- 685 Ravindra, K., Bencs, L., Wauters, E., De Hoog, J., Deutsch, F., Roekens, E., Bleux, N., Berghmans, P. and Van Grieken, R.:
Seasonal and site-specific variation in vapour and aerosol phase PAHs over Flanders (Belgium) and their relation with
anthropogenic activities, *Atmos. Environ.*, 40(4), 771–785, doi:10.1016/j.atmosenv.2005.10.011, 2006.
- Le Roy, L., Bardyn, A., Briois, C., Cottin, H., Fray, N., Thirkell, L. and Hilchenbach, M.: COSIMA calibration for the
detection and characterization of the cometary solid organic matter, *Planet. Space Sci.*, 105, 1–25,
690 doi:10.1016/j.pss.2014.08.015, 2015.
- Sadezky, A., Muckenhuber, H., Grothe, H., Niessner, R. and Pöschl, U.: Raman microspectroscopy of soot and related
carbonaceous materials: Spectral analysis and structural information, *Carbon*, 43(8), 1731–1742,
doi:10.1016/j.carbon.2005.02.018, 2005.
- Stein, S. E. and Fahr, A.: High-temperature stabilities of hydrocarbons, *J. Phys. Chem.*, 89(17), 3714–3725,
695 doi:10.1021/j100263a027, 1985.
- Sun, P., Blanchard, P., Brice, K. A. and Hites, R. A.: Trends in Polycyclic Aromatic Hydrocarbon Concentrations in the
Great Lakes Atmosphere, *Environ. Sci. Technol.*, 40(20), 6221–6227, doi:10.1021/es0607279, 2006.
- Szulejko, J. E., Kim, K. H., Brown, R. J. C. and Bae, M. S.: Review of progress in solvent-extraction techniques for the
determination of polyaromatic hydrocarbons as airborne pollutants, *TrAC - Trends Anal. Chem.*, 61, 40–48,
700 doi:10.1016/j.trac.2014.07.001, 2014.
- Villanueva, F., Sevilla, G., Lara, S., Martín, P., Salgado, S., Albaladejo, J. and Cabañas, B.: Application of gas
chromatography coupled with tandem mass spectrometry for the assessment of PAH levels in non industrial indoor air,
Microchem. J., 142, 117–125, doi:10.1016/J.MICROC.2018.06.021, 2018.
- Yon, J., Bescond, A. and Ouf, F. X.: A simple semi-empirical model for effective density measurements of fractal
705 aggregates, *J. Aerosol Sci.*, 87, 28–37, doi:10.1016/j.jaerosci.2015.05.003, 2015.
- Yon, J., Ouf, F. X., Hebert, D., Mitchell, J. B., Teuscher, N., Garrec, J. L. Le, Bescond, A., Baumann, W., Ourdani, D.,
Bizien, T. and Perez, J.: Investigation of soot oxidation by coupling LII, SAXS and scattering measurements, *Combust.
Flame*, 190, 441–453, doi:10.1016/j.combustflame.2017.12.014, 2018.
- Zíková, N., Ondráček, J. and Ždímal, V.: Size-Resolved Penetration Through High-Efficiency Filter Media Typically Used
710 for Aerosol Sampling, *Aerosol Sci. Technol.*, 49(4), 239–249, doi:10.1080/02786826.2015.1020997, 2015.